This is a repository copy of *Human contribution to the risk of 2021 Northwestern Pacific concurrent marine and terrestrial summer heat*.

White Rose Research Online URL for this paper:
https://eprints.whiterose.ac.uk/217036/

Version: Published Version

Human Contribution to the Risk of 2021 Northwestern Pacific Concurrent Marine and Terrestrial Summer Heat

Haosu Tang, Jun Wang, Yang Chen, Simon F. B. Tett, Ying Sun, Lijing Cheng, Sarah Sparrow, and Buwen Dong

AFFILIATIONS: Tang and Cheng—State Key Laboratory of Numerical Modeling for Atmospheric Sciences and Geophysical Fluid Dynamics (LASG), and International Center for Climate and Environment Sciences (ICCES), Institute of Atmospheric Physics, Chinese Academy of Sciences, and University of Chinese Academy of Sciences, Beijing, China; **Wang**—The Key Laboratory of Land Surface Pattern and Simulation, Institute of Geographical Sciences and Natural Resources Research, Chinese Academy of Sciences, Beijing, China; **Chen**—State Key Laboratory of Severe Weather, Chinese Academy of Meteorological Sciences, Beijing, China; **Tett**—School of Geosciences, University of Edinburgh, Edinburgh, United Kingdom; Sun—National Climate Center, Laboratory for Climate Studies, China Meteorological Administration, Beijing, China; **Sparrow**—Oxford e-Research Centre, Department of Engineering Science, University of Oxford, Oxford, United Kingdom; **Dong**—National Centre for Atmospheric Science, Department of Meteorology, University of Reading, Reading, United Kingdom

CORRESPONDING AUTHOR: Jun Wang, wangjun@igsnrr.ac.cn

Publisher's Note: This article was modified on 19 May 2023 to correct the In Final Form date.

Current human-induced warming has led to approximately a 30-fold increase in the occurrence probability of 2021 northwestern Pacific concurrent marine and terrestrial summer heat.

July 2021 was the warmest month ever recorded for the globe, during which several extreme weather events occurred (NOAA 2022). Less noticed but just as important, an unprecedently intense marine heatwave impacted broad swaths of the northwestern Pacific (NWP; black box in Fig. 1a; 150°E–180°, 30°–50°N) in the same month, with regional mean sea surface temperature anomalies (SSTA; relative to 1961–90) up to 1.23°C (Kuroda and Setou 2021). This marine heat caused an unprecedented outbreak of red tides off Hokkaido and decimated the local fishery industry, with direct damages totaling approximately $150 million (Kuroda et al. 2021). In the meantime, neighboring northeast Asia (NEA; blue box in Fig. 1a; 125°–145°E, 30°–45°N) experienced extreme terrestrial heat, with regional mean surface air temperature anomalies (SATA) reaching 2.32°C, making the Tokyo 2020 Olympics the hottest Olympic Games in history. This spatially concurrent marine and terrestrial heat may cause regionally compounding effects, including synchronous reductions in fishery and agricultural yields and potential impacts on food security (Zscheischler et al. 2020). This spatially compounding heat likely results from a persistent blocking high. The human influences on the occurrence risk of this
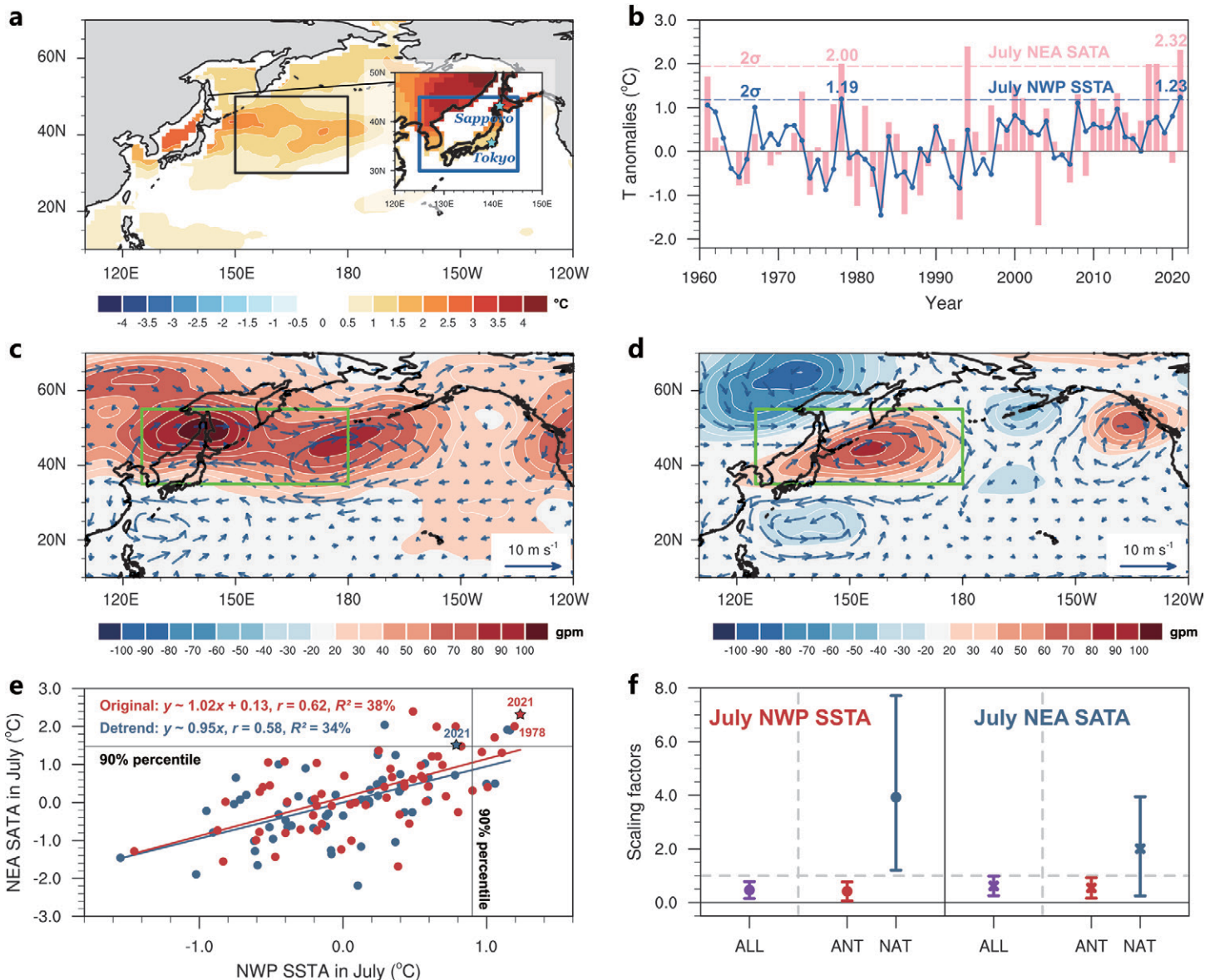
Fig. 1. (a) SSTA (°C) and SATA (inset; °C) patterns in July 2021. The main hosting cities of the 2020 Tokyo Olympics are marked by green stars. The black and blue rectangles encompass the NWP and NEA regions, respectively. (b) The July NWP SSTA (blue solid line; °C) and NEA SATA (pink bars; °C) during 1961–2021. The 2σ levels are marked by dashed lines. Values for the years 1978 and 2021 are shown as well. (c) Anomalies of July 2021 500-hPa geopotential height (with zonal mean removed; shadings; gpm) and 850-hPa horizontal wind (vectors; m s^{-1}) from ERA5. The green rectangle indicates the target circulation region. (d) As in (c), but for the year 1978. (e) Statistical dependence between July NWP SSTA and NEA SATA. Red dots indicate the original data, and blue dots the linearly detrended ones. The year 2021 is marked by stars, and the 90th percentiles are highlighted. The linear regression model, the Pearson correlation coefficient (r), and the proportion of the variance of y explained by x (R^2) are also shown. (f) The best estimate and 90% confidence interval of the scaling factors (derived from the ROF) for ALL, ANT, and NAT forcings in July NWP SSTA and NEA SATA.

compound event remain poorly understood . The goal of the present study is to answer this question by assessing whether and to what extent anthropogenic warming has contributed to the occurrence probability of the 2021 NWP concurrent marine and terrestrial summer heat (Perkins-Kirkpatrick et al. 2019; Amaya et al. 2021).

Data

We focus on July mean temperature anomalies since both marine and terrestrial heat occurred in July 2021. We find modest differences of about 0.1°C exist in July SSTA among different

datasets (Fig. ES1 in the online supplemental material). To minimize uncertainties, we calculate the ensemble mean of three monthly datasets (HadISST; Rayner et al. 2003; ERSSTv5; Smith et al. 2008; COBE-SSTv2; Hirahara et al. 2014) as the best observational SSTA estimate. We use the monthly gridded Berkeley Earth land surface temperature (BEST; Rohde et al. 2013) to calculate SATA over terrestrial NEA. We also use monthly 850-hPa horizontal wind and 500-hPa geopotential height data from the ERA5 reanalysis (Hersbach et al. 2020). We focus our analyses on 1961–2021, and the results are generally robust against different choices of studying periods and climate norms.

We use model outputs of monthly SAT, surface temperature, and geopotential heights from the CMIP6 archive to investigate the influences of anthropogenic forcings (ANT; Eyring et al. 2016). To improve the sampling of internal climate variability, we require each model to have at least three ensemble members and 500 years of preindustrial control (pi-CTL) run. Ten models satisfy this criterion, which produce historical simulations until 2014 with all forcings (ALL; hist-All) and until 2020 with natural-only forcings (NAT; hist-Nat), and future projections unfolding along two different Shared Socioeconomic Pathways (SSP2-45 and SSP5-85) (Table ES1). Since SSP2-45 forcings were employed in hist-Nat simulations for 2015–20 (Gillett et al. 2021), we extend the hist-All simulations with corresponding SSP2-45 experiments for this period. All the data are bilinearly interpolated to a $1° \times 1°$ grid from their respective original grids and the results are generally robust against different interpolation methods.

Methods

Accounting for potential biases in the simulated responses to forcings, we first perform calibration analysis using regularized optimal fingerprinting method (ROF; Allen and Stott 2003; Ribes et al. 2013). Briefly, based on a total least squares algorithm, this technique regresses the observed change onto the simulated responses to different forcings and accounts for the noise in the model responses associated with internal variability (Note ES1). After ensuring the detectability of ANT, we use the ROF-derived regression coefficient (i.e., scaling factor) of ANT to calibrate historical and future ANT signals. We add these observationally constrained ANT signals to nonoverlapping 60-yr chunks of unforced series (pi-CTL simulations) to create plausible realizations of NWP SSTA and NEA SATA (Sun et al. 2014). We compare the constructed evolutions involving anthropogenically forced warming with the unforced ones to investigate the overall contribution of human influences to the event risk. To reduce uncertainties related to statistical methods, here we use three different approaches to estimate the joint probabilities of occurrence of 2021-like spatially concurrent heat extremes with and without human influences (P_{ANT} and P_{CTL}) by

1) empirically counting the occurrence of the events with SSTA and SATA exceeding their respective thresholds (i.e., the 1978 event; Figs. 1b,e);
2) using a Gaussian copula to model the codependence of SSTA and SATA and derive bivariate exceedance probability (Nelsen 2007);
3) using a Gaussian bivariate kernel density estimator (GBKDE; Terrell and Scott 1992).

We compute the probability ratio (PR = P_{ANT}/P_{CTL}) and its 5%–95% uncertainty range via bootstrapping 1,000 times (Efron and Tibshirani 1994).

Results

Both the July 2021 NWP SSTA and NEA SATA are above two standard deviations (σ) and are the first and second warmest since 1961, respectively (Fig. 1b). The midlatitude lobe of the positive Pacific–Japan teleconnection pattern serves as a common driver of sunny and hot weather

over the subtropical NWP (Figs. 1c,d; Noh et al. 2021). As a result, the marine and terrestrial heat are significantly spatially related (Fig. 1e). Mean anomalous warm air advection from NEA land to the NWP could strengthen their correlation as well.

The ANT and NAT signals are jointly detectable in the observed SSTA and SATA changes, while the scaling factors for NAT exhibit a much larger confidence interval (Fig. 1f). The below-unity scaling factors for ANT indicate an overestimate of the amplitude of simulated regional temperature responses to ANT in models (i.e., "hot model" bias; Hausfather et al. 2022). By altering the ANT signals to best match the observed changes and adding them to the unforced simulations, we produce 154 plausible realizations of the 1961–2020 NWP SSTA and NEA SATA evolutions. The median σ of the 154 reconstructed SSTA and SATA series are 0.64° and 0.80°C, close to the observations (0.59° and 0.97°C). The median Pearson correlation between them is 0.58, consistent with the observed (0.62; Fig. 1e). These results suggest that the simulated series faithfully reproduce the observed variability and statistical dependence between NWP and NEA.

Using the unforced simulations and GBKDE, we estimate the occurrence probability of 2021-like NWP spatially concurrent marine and terrestrial summer heat without human-induced warming to be 0.14% (0.09%–0.21%) (Figs. 2a,c; Table 1). Due to the effects of historical anthropogenic warming from 1961 to 2020, the marginal probability distributions of NWP SSTA and NEA SATA shift toward high levels (Fig. 2a). The joint exceedance probability derived from the corresponding plausible realizations is 0.67% (0.53%–0.81%) and the associated PR is estimated to be 4.63 (3.21–7.31), which signifies that historical human-induced warming has already led to about a fourfold growth in the risk of 2021-like spatially concurrent heat events (Fig. 2c; Table 1). However, the background warming level around 2021 should be higher than the 1961–2020 average. Thus, we repeat the analysis but add the calibrated anthropogenic warming component over 1991–2050 (centered on 2021) to the unforced data (referred to as ANT-SSP2-45). The estimated PR increases to 32.23 (21.98–51.77), which means current human-induced warming has resulted in approximately a 30-fold increase in the

Table 1. The marginal (for SSTA and SATA, based on Gaussian fitting) and joint exceedance probability (estimated via three statistical methods) exceeding the observed 2021 thresholds in different reconstructed plausible realizations. The PRs and their corresponding 5%–95% ranges are shown as well.

| Simulations/PRs	Marginal probability (SSTA)	Marginal probability (SATA)	Joint exceedance probabilities estimated by three different statistical approaches		
			Empirical	Gaussian copula	GBKDE
I. Unforced	2.85% (2.67%–3.05%)	0.40% (0.36%–0.45%)	0.14% (0.08%–0.21%)	0.11% (0.09%–0.13%)	0.14% (0.09%–0.21%)
II. ANT (1961–2020)	6.36% (6.06%–6.73%)	1.43% (1.32%–1.55%)	0.58% (0.47%–0.71%)	0.58% (0.52%–0.63%)	0.67% (0.53%–0.81%)
PR (II/I)	2.23 (2.05–2.43)	3.57 (3.13–4.10)	4.17 (2.83–7.14)	5.20 (4.78–5.71)	4.63 (3.21–7.31)
III. ANT-SSP2-45 (1991–2050)	20.22% (19.63%–20.82%)	7.68% (7.35%–8.04%)	4.36% (3.99%–4.72%)	4.57% (4.35%–4.83%)	4.67% (4.30%–5.04%)
PR (III/I)	7.05 (6.55–7.63)	19.28 (17.02–21.82)	31.38 (21.18–55.81)	41.86 (37.76–46.75)	32.23 (21.98–51.77)
IV. SSP2-45 (2041–2100)	55.07% (54.37%–55.80%)	33.78% (33.14%–33.44%)	25.52% (24.79%–26.35%)	25.88% (25.30%–26.48%)	26.70% (25.90%–27.69%)
PR (IV/III)	2.73 (2.64–2.82)	4.40 (4.19–4.61)	5.86 (5.46–6.34)	5.66 (5.46–5.86)	5.72 (5.32–6.21)
V. SSP5-85 (2041–2100)	77.40% (76.88%–77.96%)	65.72% (65.08%–66.36%)	58.84% (58.02%–59.69%)	59.34% (58.67%–60.02%)	60.09% (59.00%–61.22%)
PR (V/III)	3.83 (3.72–3.94)	8.54 (8.16–8.93)	13.49 (12.53–14.73)	12.93 (12.38–13.63)	12.88 (11.92–14.12)
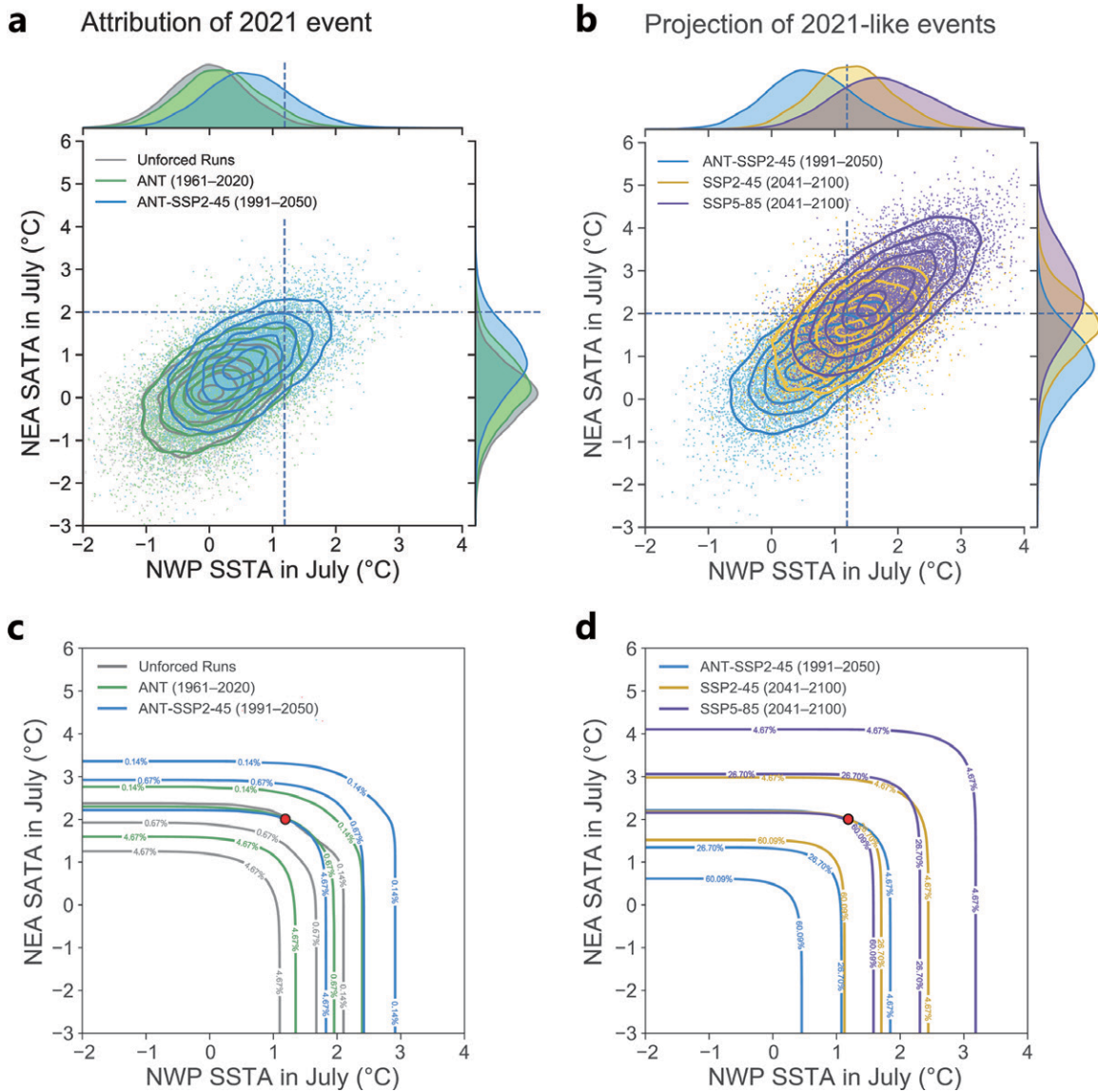
Fig. 2. (a) The marginal and joint probability distributions of July mean NWP SSTA and NEA SATA in the unforced (gray), reconstructed ANT (1961–2020, green), and ANT-SSP2-45 (1991–2050, blue) plausible realizations. The vertical and horizontal dashed lines indicate the NWP SSTA and NEA SATA thresholds (i.e., the 1978 event). From innermost to outermost, the 5th, 25th, 50th, 75th, and 95th percentiles of the distributions (contours) are estimated using a GBKDE. (b) As in (a), but for ANT-SSP2-45 (1991–2050, blue), and the reconstructed SSP2-45 (gold) and SSP5-85 (purple) plausible realizations over 2041–2100. (c) Joint occurrence risk curves for the unforced (gray), reconstructed ANT (1961–2020, green), and ANT-SSP2-45 (1991–2050, blue) plausible realizations using exceedance probabilities [i.e., $P(X > x, Y > y)$]. The colored numbers embedded in the curves represent joint exceedance probabilities. The red dot marks the joint thresholds. (d) As in (c), but for ANT-SSP2-45 (1991–2050, blue), and the reconstructed SSP2-45 (gold) and SSP5-85 (purple) plausible realizations over 2041–2100.

event's occurrence probability (Fig. 2c; Table 1). We consider the observationally constrained ANT signals over 2041–2100 (centered on 2070) to represent future warming in the second half of the twenty-first century (Figs. 2b,d). Compared to the current level, future similar events would become approximately 6- and 13-fold more likely under SSP2-45 and SSP5-85, respectively (Table 1). The 2021-like spatially concurrent summer heat would become roughly once-in-4-years and once-in-1.5-years events in these scenarios, respectively. Similar conclusions can be drawn from the other two statistical approaches, albeit with some quantitative differences (Table 1).

The increases in the frequency of 2021-like spatially compounding heat events may primarily arise from shifts in marginal distribution of NWP SSTA and NEA SATA, with the changing dependence structure contributing little (Figs. 2a,b). This connotes that their physical linkage via the common anticyclonic pattern has not been and would not be changed by anthropogenic warming. To test this hypothesis, we compute the pattern correlation coefficients (r) between July 2021 500-hPa geopotential height anomalies (with zonal mean removed; Z500$'$) from ERA5 and July Z500$'$ from hist-All (hist-Nat, SSP2-45) simulations during a 60-yr period over the target circulation region (green box in Fig. 1c; 125°E–180°, 35°–55°N). The composite circulations in the analog Z500$'$ patterns that resemble the observed in July 2021 ($r \geq 0.5$) bear notable similarities among the hist-All, hist-Nat, and SSP2-45 ensembles (Figs. ES2a–c). Moreover, there is no significant shift in the frequency of analog Z500$'$ patterns ($r \geq 0.5$) due to historical and future anthropogenic forcings (Fig. ES2d). Similar results could be achieved when directly comparing the July Z500$'$ averaged over the target circulation region in the hist-All, hist-Nat, and SSP2-45 simulations (Fig. ES2e). In addition, the result is robust against slightly changed target circulation regions and different reanalysis data (figure omitted).

Conclusions

With the aid of CMIP6 multimodel ensemble simulations and optimal fingerprinting method, we find that current human-induced warming has led to about a 30-fold increase in the occurrence probability of a record-breaking spatially concurrent marine and terrestrial summer heat that occurred across the NWP in July 2021. Its occurrence risk in the second half of the twenty-first century is projected to be at least 6 times the 2020s level, even under a moderate emission scenario. Results imply that the compounding effects of unprecedented spatially simultaneous heat on agricultural and fishery productions in the NWP and its nearby lands may increase and substantial cuts in emissions are paramount to reduce the risks. This study may shed light on the ongoing efforts attributing less explored yet potentially more impactful spatially compounding events to anthropogenic climate change.

Data availability statement. All the data that support the findings are publicly available. The gridded Berkeley Earth Surface Temperature dataset is available at http://berkeleyearth.org/data. The HadISST, ERSST v5, and COBESST v2 datasets can be downloaded from their official websites https://www.metoffice.gov.uk/hadobs/hadisst/, https://data.noaa.gov/dataset/dataset/noaa-extended-reconstructed-sea-surface-temperature-ersst-version-5, and https://data.noaa.gov/dataset/dataset/cobe-sst2-sea-surface-temperature-and-ice, respectively. The model outputs in CMIP6 can be accessed at https://esgf-node.llnl.gov/projects/cmip6/. The ERA5 reanalysis data can be secured from https://www.ecmwf.int/en/forecasts/datasets/reanalysis-datasets/era5 on registration.

References

Allen, M. R., and P. A. Stott, 2003: Estimating signal amplitudes in optimal finger-printing, part I: Theory. *Climate Dyn.*, **21**, 477–491, https://doi.org/10.1007/s00382-003-0313-9.

Amaya, D. J., M. A. Alexander, A. Capotondi, C. Deser, K. B. Karnauskas, A. J. Miller, and N. J. Mantua, 2021: Are long-term changes in mixed layer depth influencing North Pacific marine heatwaves? *Bull. Amer. Meteor. Soc.*, **102**, S59–S66, https://doi.org/10.1175/BAMS-D-20-0144.1.

Efron, B., and R. Tibshirani, 1994: *An Introduction to the Bootstrap*. CRC Press, 456 pp.

Eyring, V., S. Bony, G. A. Meehl, C. A. Senior, B. Stevens, R. J. Stouffer, and K. E. Taylor, 2016: Overview of the Coupled Model Intercomparison Project Phase 6 (CMIP6) experimental design and organization. *Geosci. Model Dev.*, **9**, 1937–1958, https://doi.org/10.5194/gmd-9-1937-2016.

Gillett, N. P., and Coauthors, 2021: Constraining human contributions to observed warming since the pre-industrial period. *Nat. Climate Change*, **11**, 207–212, https://doi.org/10.1038/s41558-020-00965-9.

Hausfather, Z., K. Marvel, G. A. Schmidt, J. W. Nielsen-Gammon, and M. Zelinka, 2022: Climate simulations: Recognize the 'hot model' problem. *Nature*, **605**, 26–29, https://doi.org/10.1038/d41586-022-01192-2.

Hersbach, H., and Coauthors, 2020: The ERA5 global reanalysis. *Quart. J. Roy. Meteor. Soc.*, **146**, 1999–2049, https://doi.org/10.1002/qj.3803.

Hirahara, S., M. Ishii, and Y. Fukuda, 2014: Centennial-scale sea surface temperature analysis and its uncertainty. *J. Climate*, **27**, 57–75, https://doi.org/10.1175/JCLI-D-12-00837.1.

Kuroda, H., and T. Setou, 2021: Extensive marine heatwaves at the sea surface in the northwestern Pacific Ocean in summer. *Remote Sens.*, **13**, 3989, https://doi.org/10.3390/rs13193989.

Kuroda, H., T. Azumaya, T. Setou, and N. Hasegawa, 2021: Unprecedented outbreak of harmful algae in Pacific coastal waters off southeast Hokkaido, Japan, during late summer 2021 after record-breaking marine heatwaves. *J. Mar. Sci. Eng.*, **9**, 1335, https://doi.org/10.3390/jmse9121335.

Nelsen, R. B., 2007: *An Introduction to Copulas*. Springer, 272 pp.

NOAA, 2022: State of the climate: Monthly global climate report for July 2021. NOAA/NCEI, accessed 17 May 2022, https://www.ncei.noaa.gov/access/monitoring/monthly-report/global/202107.

Noh, E., J. Kim, S.-Y. Jun, D.-H. Cha, M.-S. Park, J.-H. Kim, and H.-G. Kim, 2021: The role of the Pacific-Japan pattern in extreme heatwaves over Korea and Japan. *Geophys. Res. Lett.*, **48**, e2021GL093990, https://doi.org/10.1029/2021GL093990.

Perkins-Kirkpatrick, S. E., A. D. King, E. A. Cougnon, N. J. Holbrook, M. R. Grose, E. C. J. Oliver, S. C. Lewis, and F. Pourasghar, 2019: The role of natural variability and anthropogenic climate change in the 2017/18 Tasman Sea marine heatwave [in "Explaining Extreme Events of 2017 from a Climate Perspective"]. *Bull. Amer. Meteor. Soc.*, **100** (1), S105–S110, https://doi.org/10.1175/BAMS-D-18-0116.1.

Rayner, N., D. E. Parker, E. B. Horton, C. K. Folland, L. V. Alexander, D. P. Rowell, E. C. Kent, and A. Kaplan, 2003: Global analyses of sea surface temperature, sea ice, and night marine air temperature since the late nineteenth century. *J. Geophys. Res.*, **108**, 4407, https://doi.org/10.1029/2002JD002670.

Ribes, A., S. Planton, and L. Terray, 2013: Application of regularised optimal fingerprinting to attribution. Part I: Method, properties and idealised analysis. *Climate Dyn.*, **41**, 2817–2836, https://doi.org/10.1007/s00382-013-1735-7.

Rohde, R., and Coauthors, 2013: A new estimate of the average earth surface land temperature spanning 1753 to 2011. *Geoinfor. Geostat.*, **1**, 1–7, https://doi.org/10.4172/2327-4581.1000101.

Smith, T. M., R. W. Reynolds, T. C. Peterson, and J. Lawrimore, 2008: Improvements to NOAA's historical merged land-ocean surface temperature analysis (1880–2006). *J. Climate*, **21**, 2283–2296, https://doi.org/10.1175/2007JCLI2100.1.

Sun, Y., X. Zhang, F. W. Zwiers, L. Song, H. Wan, T. Hu, H. Yin, and G. Ren, 2014: Rapid increase in the risk of extreme summer heat in eastern China. *Nat. Climate Change*, **4**, 1082–1085, https://doi.org/10.1038/nclimate2410.

Terrell, G. R., and D. W. Scott, 1992: Variable kernel density estimation. *Ann. Stat.*, **20**, 1236–1265, https://doi.org/10.1214/aos/1176348768.

Zscheischler, J., and Coauthors, 2020: A typology of compound weather and climate events. *Nat. Rev. Earth Environ.*, **1**, 333–347, https://doi.org/10.1038/s43017-020-0060-z.